Two-Component Dark Matter

Bohdan GRZADKOWSKI
University of Warsaw

- Motivations
- The model
- Boltzmann equations: numerical and analytical solutions
- The relic abundance
- Direct detection
- Conclusions

◇ Subhadittya Bhattacharya, Aleksandra Drozd, B.G. and Jose Wudka "Two-Component Dark Matter", in progress,

◇ Aleksandra Drozd, B.G., Jose Wudka, "Multi-Scalar-Singlet Extension of the Standard Model - the Case for Dark Matter and an Invisible Higgs Boson", JHEP 1204 (2012) 006, arXiv:1112.2582

Motivations

- Multi-component DM seems to be a viable option as the SM contains a few "components"
- Implications of interactions between DM components
- More flexibility while fitting existing constraints ($\Omega_{DM}h^2$ and $\sigma_{DM\ N}$)

The model

Assumptions:

- Scalar φ and fermion ν DM
- φ and ν stable by a virtue of symmetry $\mathcal{G}$
- SM neutral under $\mathcal{G}$
- Non-trivial interaction between the two components
- Dim 4 interactions only

then

$$\mathcal{L}_{\rm int} = \mathcal{O}_{SM}\mathcal{O}_{DM} + \mathcal{L}_{DM}$$

$\mathcal{G} = \mathbb{Z}_2 \times \mathbb{Z}_2$ to stabilize DM components: φ and ν,

$$\varphi \sim (-,-) \quad \nu \sim (+,-) \quad \nu_h \sim (-,+)$$

where $\nu = \nu^C$ and $\nu_h = \nu_h^C$.

The most general, gauge- and $\mathcal{G}$-symmetric renormalizable potential:

$$V(H,\varphi) = -\mu_H^2 H^\dagger H + \lambda_H (H^\dagger H)^2 + \frac{1}{2}\mu_\varphi^2 \varphi^2 + \frac{1}{4!}\lambda_\varphi \left(\varphi^2\right)^2 + \lambda_x H^\dagger H \varphi^2 \,,$$

- $\langle H \rangle = \left(\begin{array}{c} 0 \\ \frac{v}{\sqrt{2}} \end{array} \right)$, with $v = 246$ GeV,
- We require the $\mathcal{G}$ symmetry to remain unbroken, so $\mu_\varphi^2 > 0$, so $\langle \varphi \rangle = 0$,
- $\langle \varphi \rangle = 0$ implies no mass-mixing between φ and H.

Mass eigenstates:

$$m_H{}^2 = -\mu_H^2 + 3\lambda_H v^2 = 2\mu_H^2 \qquad \text{and} \qquad m_\varphi^2 = \mu_\varphi^2 + \lambda_x v^2$$

$\mathcal{G} = \mathbb{Z}_2 \times \mathbb{Z}_2$ to stabilize DM components: φ and ν,

$$\varphi \sim (-,-) \quad \nu_h \sim (-,+) \quad \nu \sim (+,-)$$

- The extra fermionic Lagrangian:

$$\mathcal{L} = \frac{1}{2}\overline{\nu_h}\, i\partial\!\!\!/\, \nu_h + \frac{1}{2}\overline{\nu}\, i\partial\!\!\!/\, \nu - \frac{1}{2}\nu_h^T C \nu_h M_h - \frac{1}{2}\nu^T C \nu m_\nu + g_\nu \varphi\, \overline{\nu_h}\nu.$$

- Interaction between the SM and DM and the DM self-interactions:

$$\mathcal{L}_{\rm int} = -\lambda_x H^\dagger H \varphi^2 + g_\nu \varphi\, \overline{\nu_h}\nu$$

- No interactions between ν_h, ν and SM

Theoretical constraints:

$$V(H,\varphi) = -\mu_H^2 H^\dagger H + \lambda_H (H^\dagger H)^2 + \frac{1}{2}\mu_\varphi^2 \varphi^2 + \frac{1}{4!}\lambda_\varphi \left(\varphi^2\right)^2 + \lambda_x H^\dagger H \varphi^2$$

- Vacuum stability:

$$\lambda_\varphi > 0\,; \quad \lambda_x > -\sqrt{\frac{\lambda_\varphi \lambda_H}{6}} = -\frac{m_h}{2v}\sqrt{\frac{\lambda_\varphi}{3}}\,.$$

- Tree-level unitarity:

$$\lambda_\varphi < 8\pi, \qquad |\lambda_x| < 4\pi\,.$$

- Perturbativity:

$$\lambda_\varphi < 4\pi, \qquad |\lambda_x| < 4\pi, \qquad |g_\nu| < 4\pi$$

$$V(H,\varphi) = -\mu_H^2 H^\dagger H + \lambda_H (H^\dagger H)^2 + \frac{1}{2}\mu_\varphi^2\varphi^2 + \frac{1}{4!}\lambda_\varphi \left(\varphi^2\right)^2 + \lambda_x H^\dagger H \varphi^2$$

Since $\mu_\varphi^2 > 0$ and $m_\varphi^2 = \mu_\varphi^2 + \lambda_x v^2$, therefore if $\lambda_x > 0$ then

$$m_\varphi^2 > \lambda_x v^2\,;$$

as a consequence, light scalars ($m_\varphi \ll v$) must couple very weakly to the SM:
The above constraints imply that, the following regions are allowed:

$$0 < \lambda_x < \min\left[\left(\tfrac{m_\varphi}{v}\right)^2, 4\pi\right]$$

$$-0.74 < -\tfrac{m_h}{2v}\sqrt{\tfrac{\lambda_\varphi}{3}} < \lambda_x < 0,$$

where the maximal value of $\lambda_\varphi = 8\pi$ consistent with unitarity was adopted.

$$\mathcal{L}_{\rm int} = -\lambda_x H^\dagger H \varphi^2 + g_\nu \varphi\, \overline{\nu_h}\nu$$

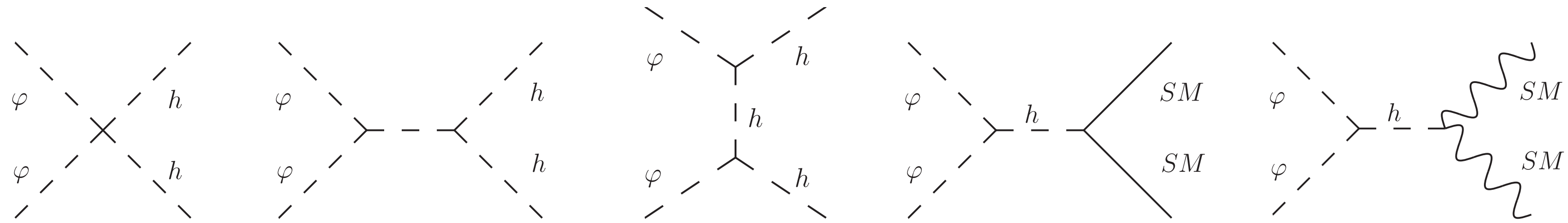

Figure 1: Diagrams contributing to the scalar $\varphi\varphi$ annihilation into SM particles.

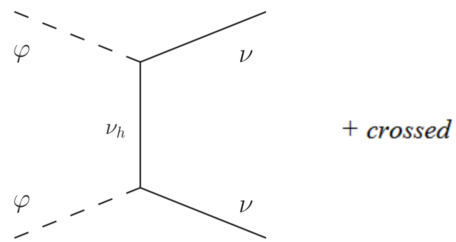

Figure 2: Diagrams contributing to the scalar $\varphi\varphi$ annihilation into DM neutrinos.

Parameters:

- λ_x, g_ν, m_ν and m_φ
- M_h - mass of the heavy "neutrino" assumed to be $M_h = m_\nu + m_\varphi + 10$ GeV

Boltzmann equations: numerical and analytical solutions

$$\begin{aligned}\dot{n}_\varphi + 3Hn_\varphi &= -\langle\sigma_{\varphi\varphi\to SM\,SM}v\rangle\left(n_\varphi^2 - n_\varphi^{EQ2}\right) - \left(\langle\sigma_{\varphi\varphi\to\nu\nu}v\rangle n_\varphi^2 - \langle\sigma_{\nu\nu\to\varphi\varphi}v\rangle n_\nu^2\right)\\ \dot{n}_\nu + 3Hn_\nu &= -\left(\langle\sigma_{\nu\nu\to\varphi\varphi}v\rangle n_\nu^2 - \langle\sigma_{\varphi\varphi\to\nu\nu}v\rangle n_\varphi^2\right)\end{aligned}$$

where

$$\begin{aligned}\langle\sigma_{XX\to YY}v\rangle(T) &\equiv \frac{1}{\left(n_X^{EQ}\right)^2}\int\frac{\zeta_X d^3p}{(2\pi)^3 2E_p}\frac{\zeta_X d^3p'}{(2\pi)^3 2E'_p}\frac{\zeta_Y d^3q}{(2\pi)^3 2E_q}\frac{\zeta_Y d^3q'}{(2\pi)^3 2E'_q}\times\\ &\quad\delta^4(p+p'-q-q')|M_{XX\to YY}|^2 e^{-(E_p+E'_p)/T}\end{aligned}$$

and

$$\langle\sigma_{\nu\nu\to\varphi\varphi}v\rangle = \left(\frac{n_\varphi^{EQ}}{n_\nu^{EQ}}\right)^2\langle\sigma_{\varphi\varphi\to\nu\nu}v\rangle$$

The solutions can be classified according to the mass hierarchy in the dark sector:

Case A: $m_\nu > m_\varphi$, Case B: $m_\nu < m_\varphi$

$$f_X(T) \equiv \frac{n_X(T)}{T^3} \qquad \text{for} \qquad X = \nu, \varphi$$

The case A ($m_\nu > m_\varphi$)

$$\begin{aligned} f'_\varphi &= \sigma(T)\left[f_\varphi^2 - {f_\varphi^{EQ}}^2\right] + \sigma_A(T)\left[\left(\frac{f_\nu^{EQ}}{f_\varphi^{EQ}}\right)^2 f_\varphi^2 - f_\nu^2\right] \\ f'_\nu &= \sigma_A(T)\left[f_\nu^2 - \left(\frac{f_\nu^{EQ}}{f_\varphi^{EQ}}\right)^2 f_\varphi^2\right], \end{aligned}$$

where

$$\begin{aligned} \sigma(T) &\propto \langle \sigma_{\varphi\varphi \to SM\,SM} v \rangle(T) = \text{const} + \mathcal{O}(T) \\ \sigma_A(T) &\propto \langle \sigma_{\nu\nu \to \varphi\varphi} v \rangle(T) = aT + \mathcal{O}(T^2) \end{aligned}$$

$$\delta_\varphi^A \simeq 2.3\% \qquad \delta_\varphi^A \simeq 1.4\%$$

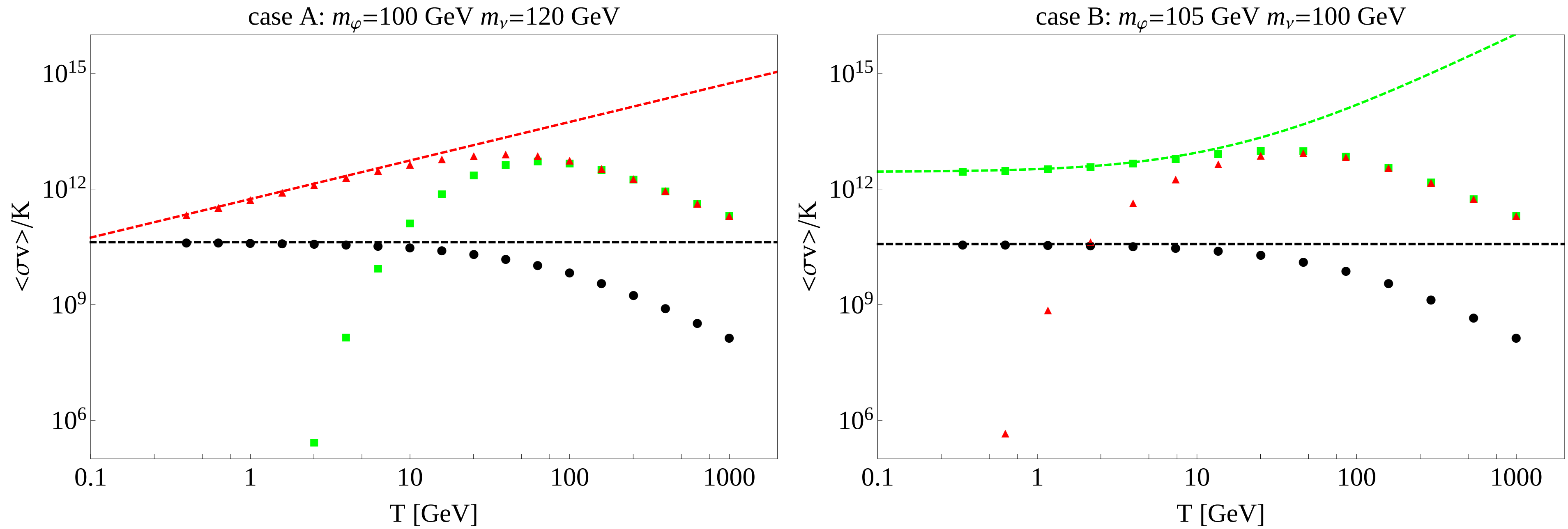

Figure 3: Thermally averaged cross sections $\langle\sigma_{\varphi\varphi\to SM\,SM} v\rangle/K$ (black points); $\langle\sigma_{\varphi\varphi\to\nu\nu} v\rangle/K$ (green points); $\langle\sigma_{\nu\nu\to\varphi\varphi} v\rangle/K$ (red points), as a functions of T (in GeV), for $\lambda_x = .1$ and $g_\nu = 2.5$. In the left panel: $m_\varphi = 100$ GeV, $m_\nu = 120$ GeV (case A); in the right panel: $m_\varphi = 120$ GeV, $m_\nu = 100$ GeV (case B).

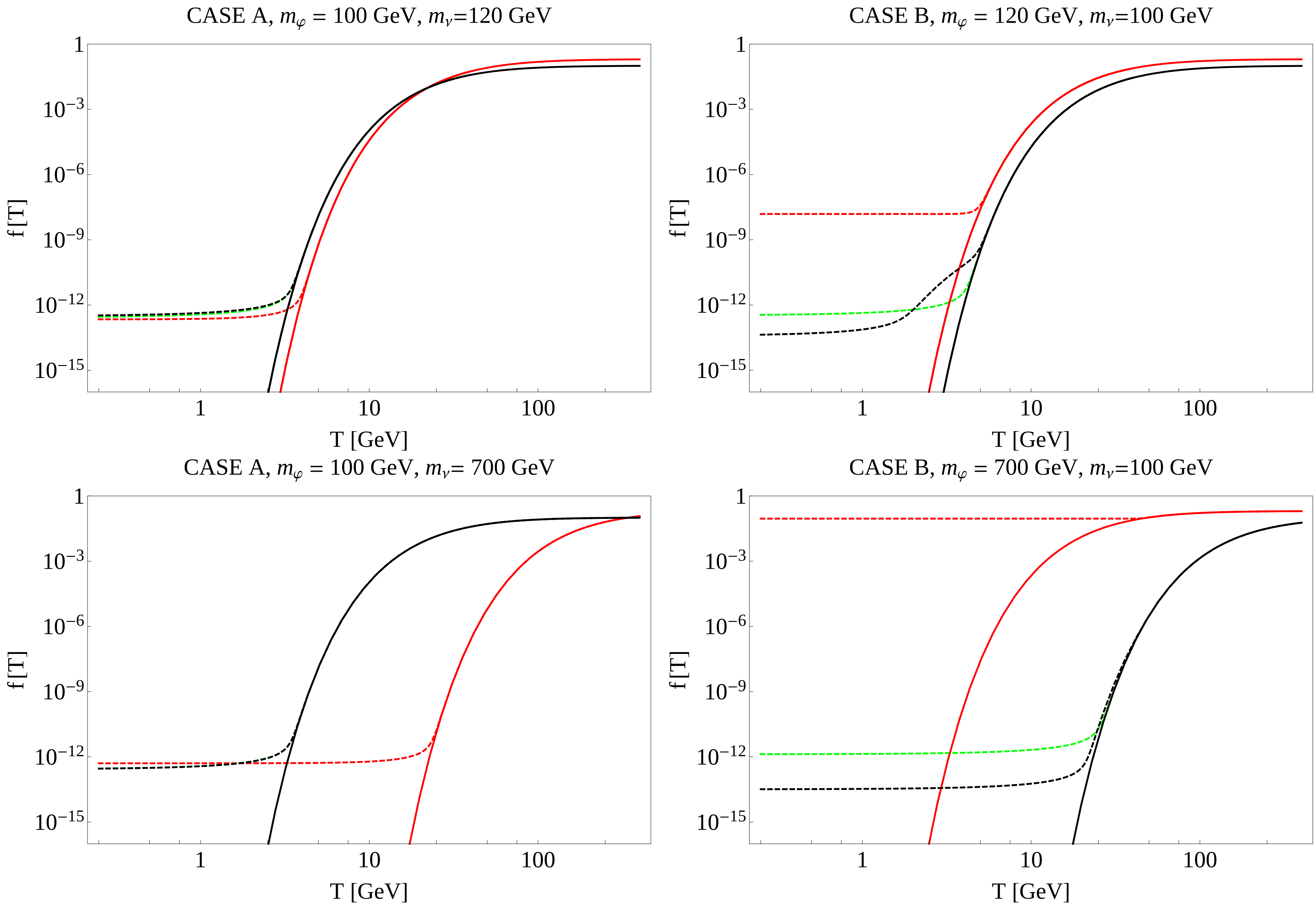

Figure 4: Solutions to the BEQs for $f_X(T) \equiv n_X(T)/T^3$ for case A (left panels) and case B (right panels) for $\lambda_x = 0.1$ and $g_\nu = 2.5$. Solid black (red) lines correspond to the equilibrium distributions, f_φ^{EQ} (f_ν^{EQ}) for scalars (neutrinos), dashed lines are the corresponding numerical solutions of the BEQs. Green dashed lines show numerical solutions of a single BEQ for scalars without neutrinos present in the theory.

$$\Delta_\varphi \equiv f_\varphi - f_\varphi^{EQ}, \qquad \Delta_\nu \equiv f_\nu - f_\nu^{EQ}$$

$$\Delta_\nu(T) \simeq \frac{\Delta_\nu(T_f^\nu)}{1 - \Delta_\nu(T_f^\nu)\int_{T_f^\nu}^{T}\sigma_A dT} \quad \Rightarrow \quad f_\nu(T_{CMB}) \simeq \frac{2}{\sigma_A(T_f^\nu)T_f^\nu}$$

$$\Delta_\varphi(T) \simeq \frac{r_f}{\sigma T_f^\varphi}\frac{u + \tanh[r_f(1 - T/T_f^\varphi)]}{1 + u\tanh[r_f(1 - T/T_f^\varphi)]}; \qquad \Rightarrow \quad f_\varphi(T_{CMB}) \simeq \frac{1}{\sigma T_f^\varphi}$$

for

$$r_f = \frac{T_f^\varphi}{T_f^\nu}\sqrt{\frac{\sigma}{\sigma_A(T_f^\varphi)}}, \; u = \frac{c_\varphi m_\varphi}{r_f T_f^\varphi}$$

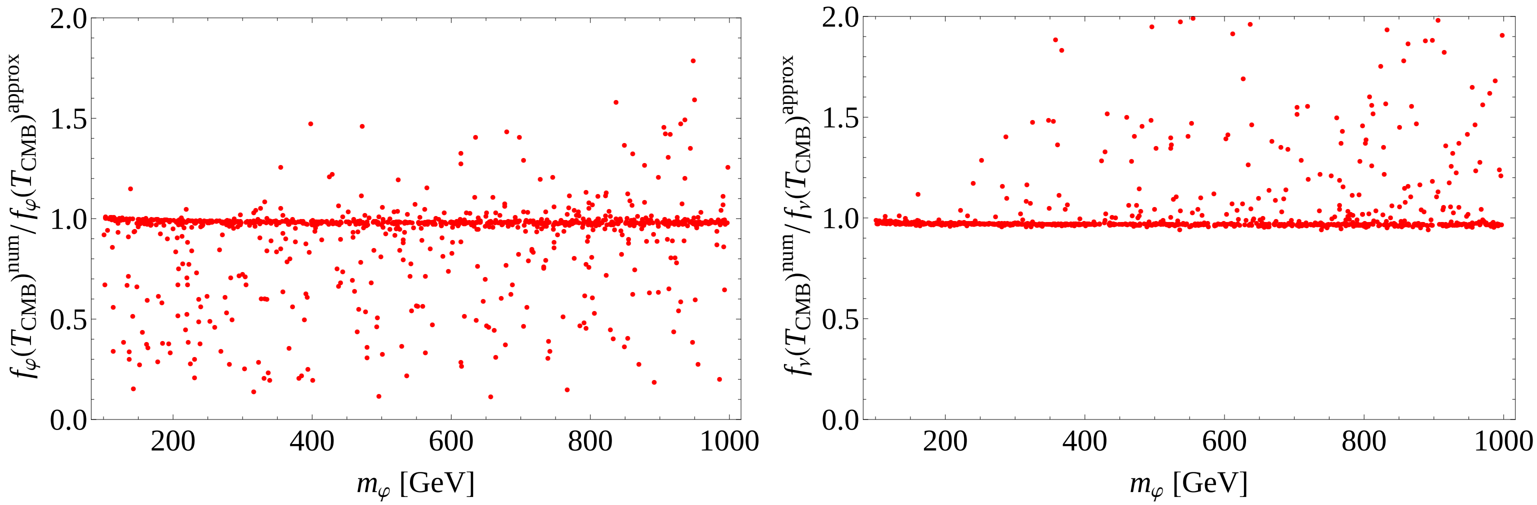

Figure 5: The ratio $f_X(T_{\rm CMB})^{\rm num}/f_X(T_{\rm CMB})^{\rm approx}$ for case A for scalars (left panel) and neutrinos (right panel). The parameters $m_\varphi, m_\nu, \lambda_x, g_\nu$ were chosen randomly within the range 10 GeV $< m_\varphi, m_\nu <$ 2 TeV, $0.001 < \lambda_x < 4\pi$ and $0.1 < g_\nu < 4\pi$.

The relic abundance

$$\Omega_{tot} = \Omega_\nu + \Omega_\varphi = \frac{m_\nu f_\nu + m_\varphi f_\varphi}{\rho_{crit}} T^3_{CMB}$$

$$\Omega_{\rm WMAP} h^2 = 0.1138 \pm 0.0045$$

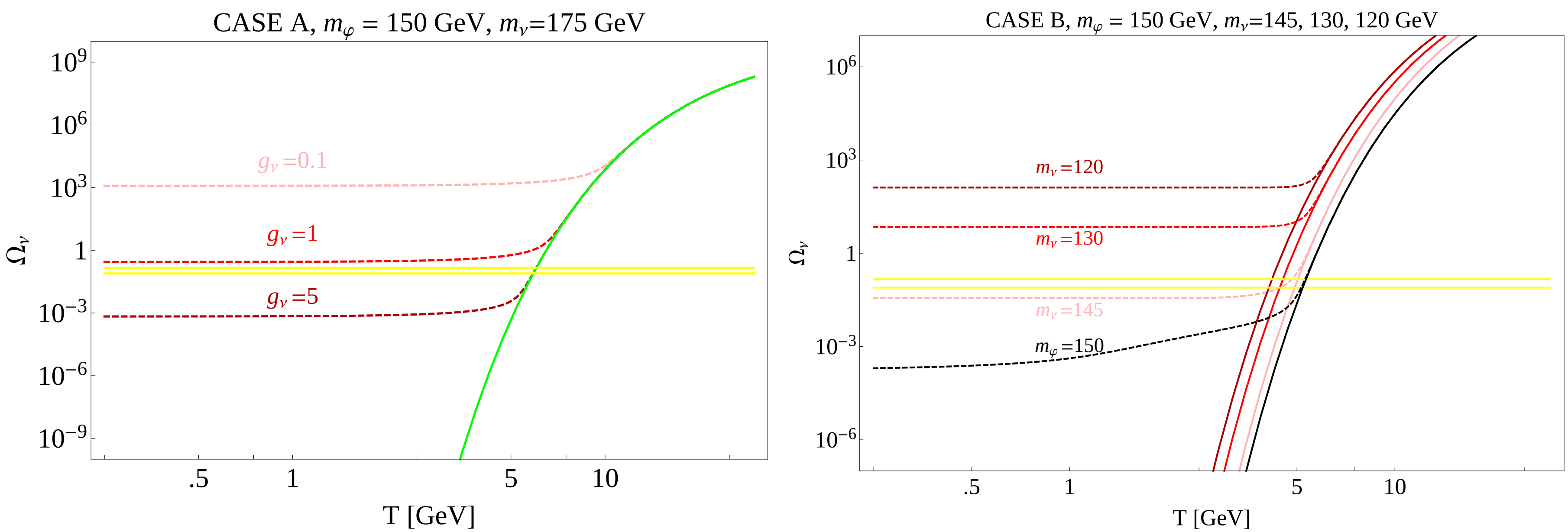

Figure 6: Left panel: solutions of the BEQs for $m_\varphi = 150$ GeV, $m_\nu = 175$ GeV (case A), $\lambda_x = 1$. Pink, red, dark red lines: solutions for the neutrino abundance for $g_\nu = 0.1, 1, 10$, respectively. Green: equilibrium distribution for neutrinos at 175 GeV. Right panel: solutions to the BEQs: f_φ (dashed black line), f_φ^{EQ} (solid black line) and f_ν for $m_\nu = 145, 130, 120$ GeV (light red, red and dark red dashed lines, respectively), In all cases we chose $m_\varphi = 150$ GeV, $\lambda_x = 1$, $g_\nu = 7.5$. Yellow lines are from the WMAP 6σ allowed region of DM abundance.

1 GeV $< m_\varphi <$ 10 TeV, 1 GeV $< m_\nu <$ 2 TeV, $0.001 < |\lambda_x| < 4\pi$, $0.1 < g_\nu < 4\pi$

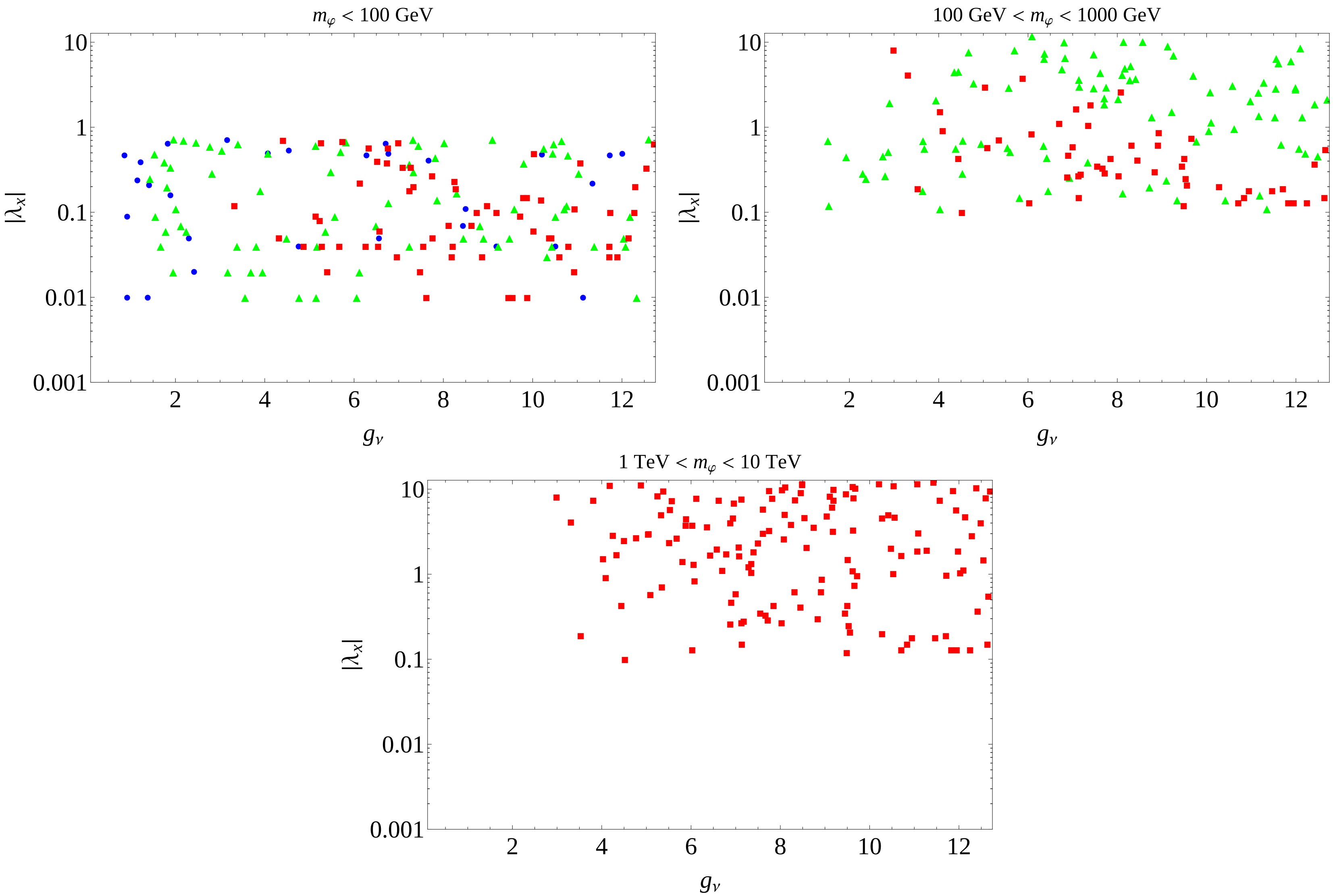

Figure 7: Points (obtained by solving the BEQs numerically) that satisfy WMAP bound for cases A and B and projected into the (λ_x, g_ν) plane. Blue (circles): $m_\nu < 100$ GeV, green (triangles): 100 GeV $< m_\nu < 1$ TeV red (squares): 1 TeV $< m_\nu < 2$ TeV and for scalar DM mass ranges as indicated in each panel.

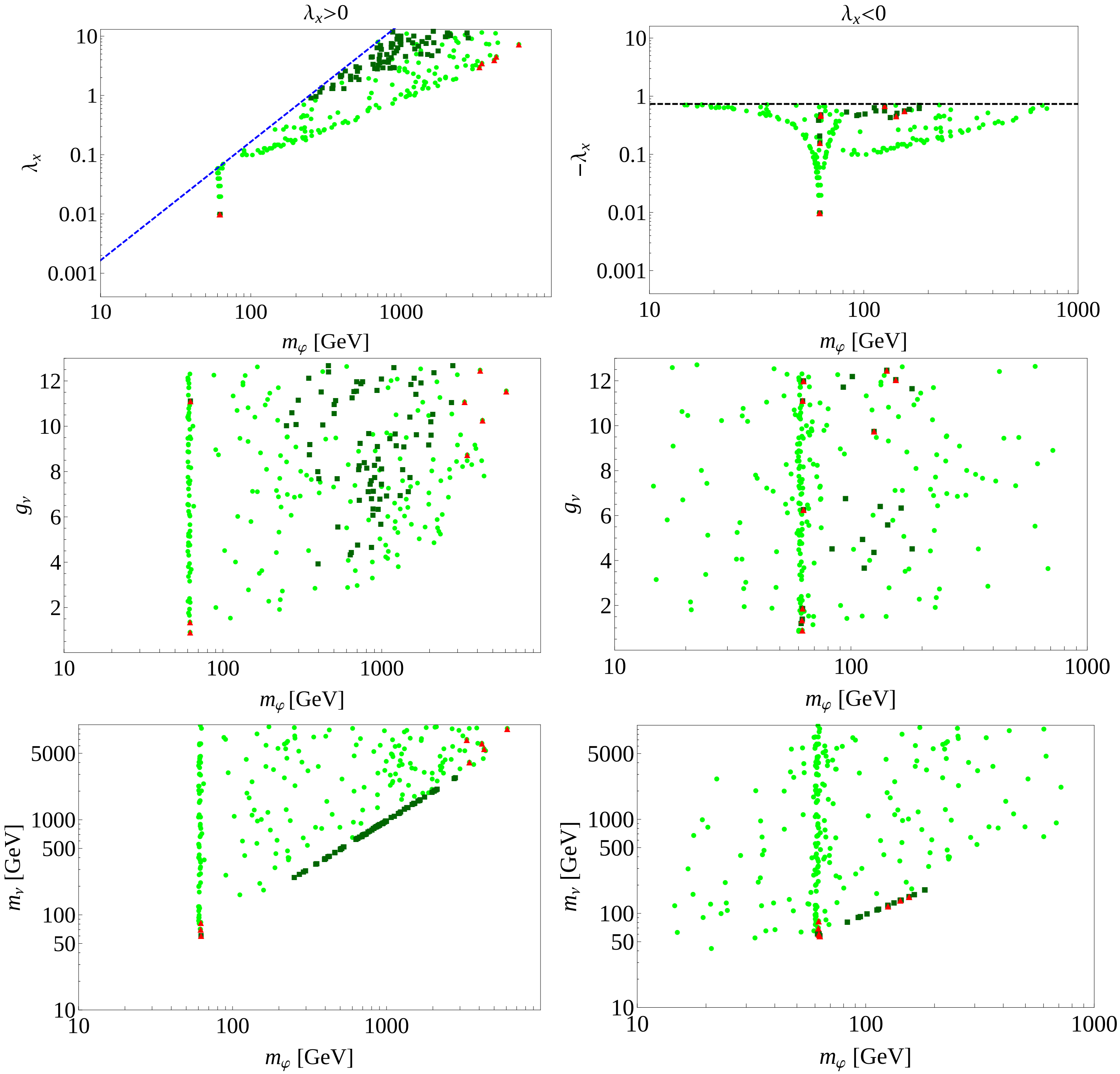

Figure 8: Points that satisfy WMAP bound within 6σ range projected into (λ_x, m_φ) (upper), (g_ν, m_φ) (middle) and (m_ν, m_φ) (lower) planes. Green circles - case A points, dark green squares - case B points. Red triangles - points that also satisfy XENON100 limit. Blue diamonds - points that also satisfy CRESST limit.

Direct Detection

$$\sigma_{\mathrm{DM-N}} = \frac{n_\varphi}{n_\varphi + n_\nu}\sigma_{\varphi N} = \frac{n_\varphi}{n_\varphi + n_\nu}\left(\frac{\lambda_x}{m_\varphi}\right)^2 \frac{v^2 m_n^2 \left(\sum_q f_q^N\right)^2}{\pi m_h^4}$$

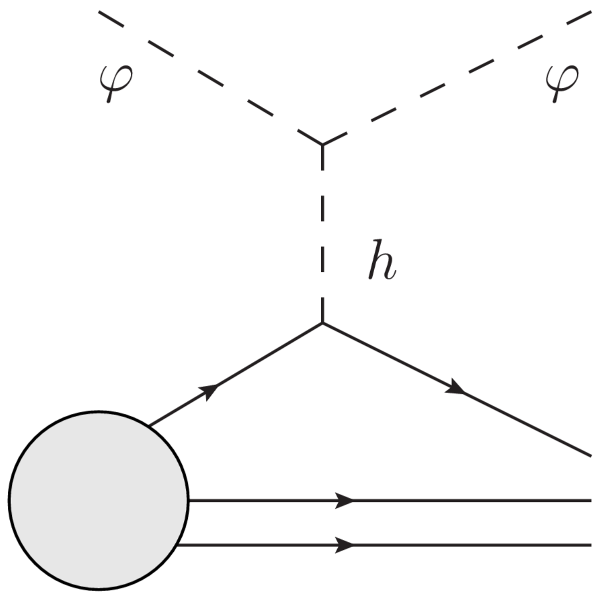

Figure 9: The Feynman diagram for the elastic scattering of φ off a nucleon.

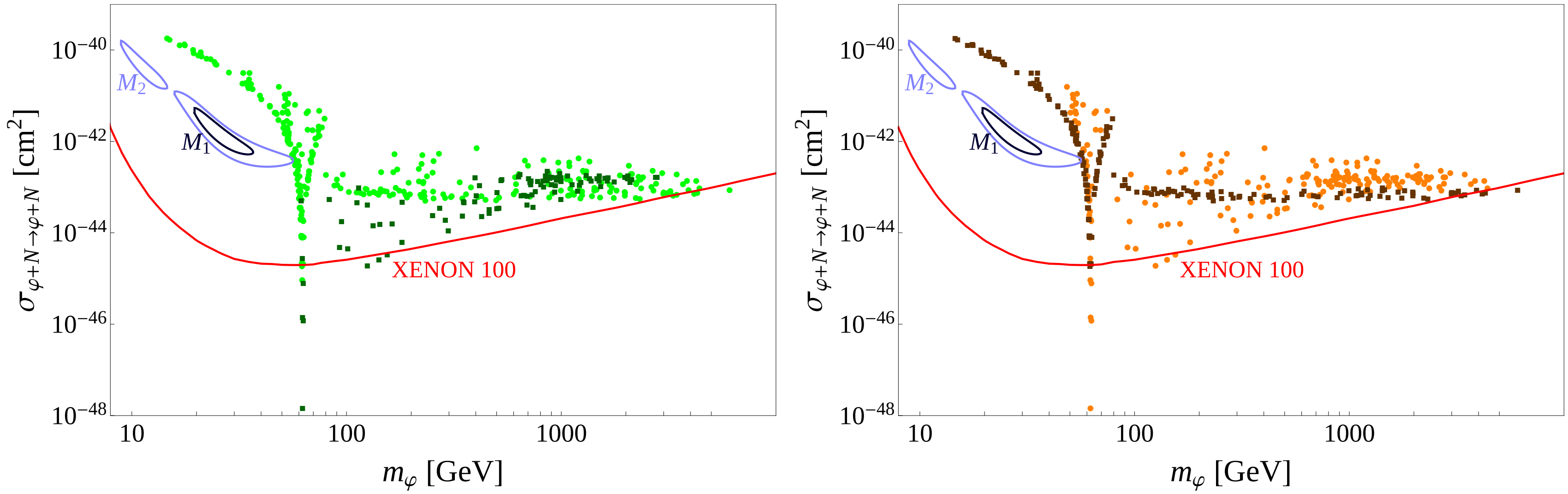

Figure 10: $\sigma_{\rm DM-N}$ as a function of the scalar mass m_φ for points satisfying the WMAP data within 6σ. Left panel: green circles (dark green squares) correspond to case A (case B) solutions. Right panel: orange circles (dark orange squares) correspond to $\Omega_\varphi < \Omega_\nu$ ($\Omega_\varphi > \Omega_\nu$). The red line shows the XENON100 data, and the two islands in blue indicate 1 and 2σ CRESST-II results.

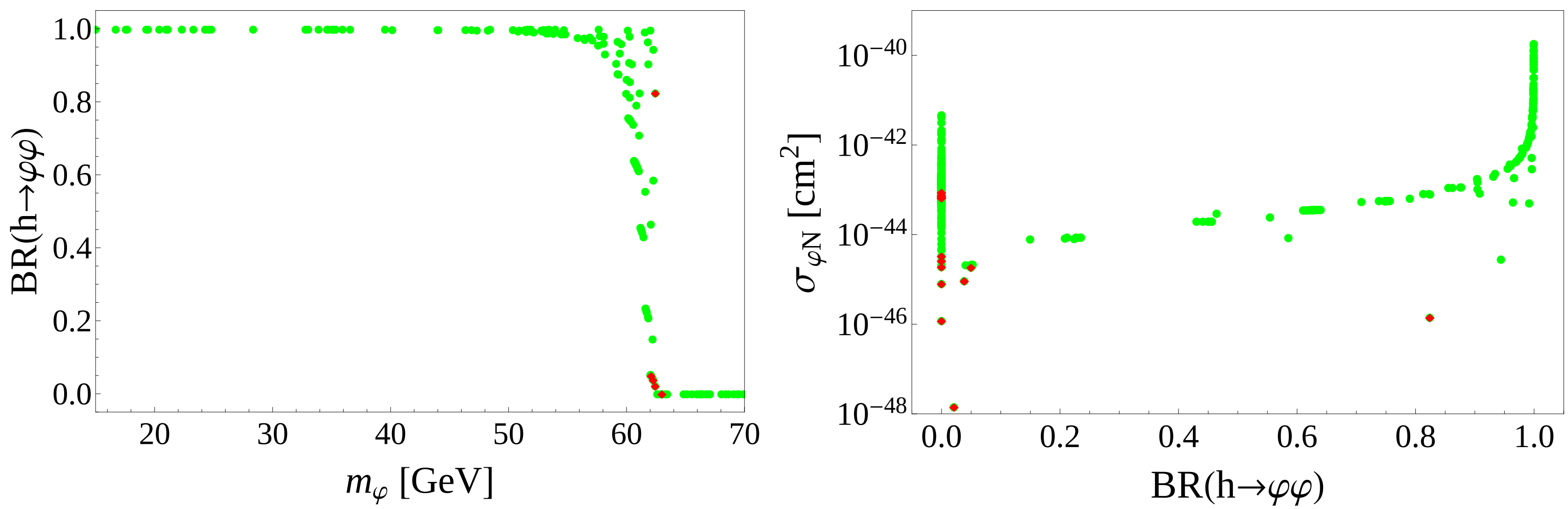

Figure 11: Left panel: plot of the invisible branching ratio $BR(h \to \varphi\varphi)$ as a function of the scalar mass m_φ. Right panel: plot of the cross section $\sigma_{\varphi N}$ against $BR(h \to \varphi\varphi)$. Green circles: points that satisfy also the WMAP data with 6σ range; red triangles: points that satisfy the XENON100 limit; blue diamonds: points that agree with the CREST-II $M1$ data.

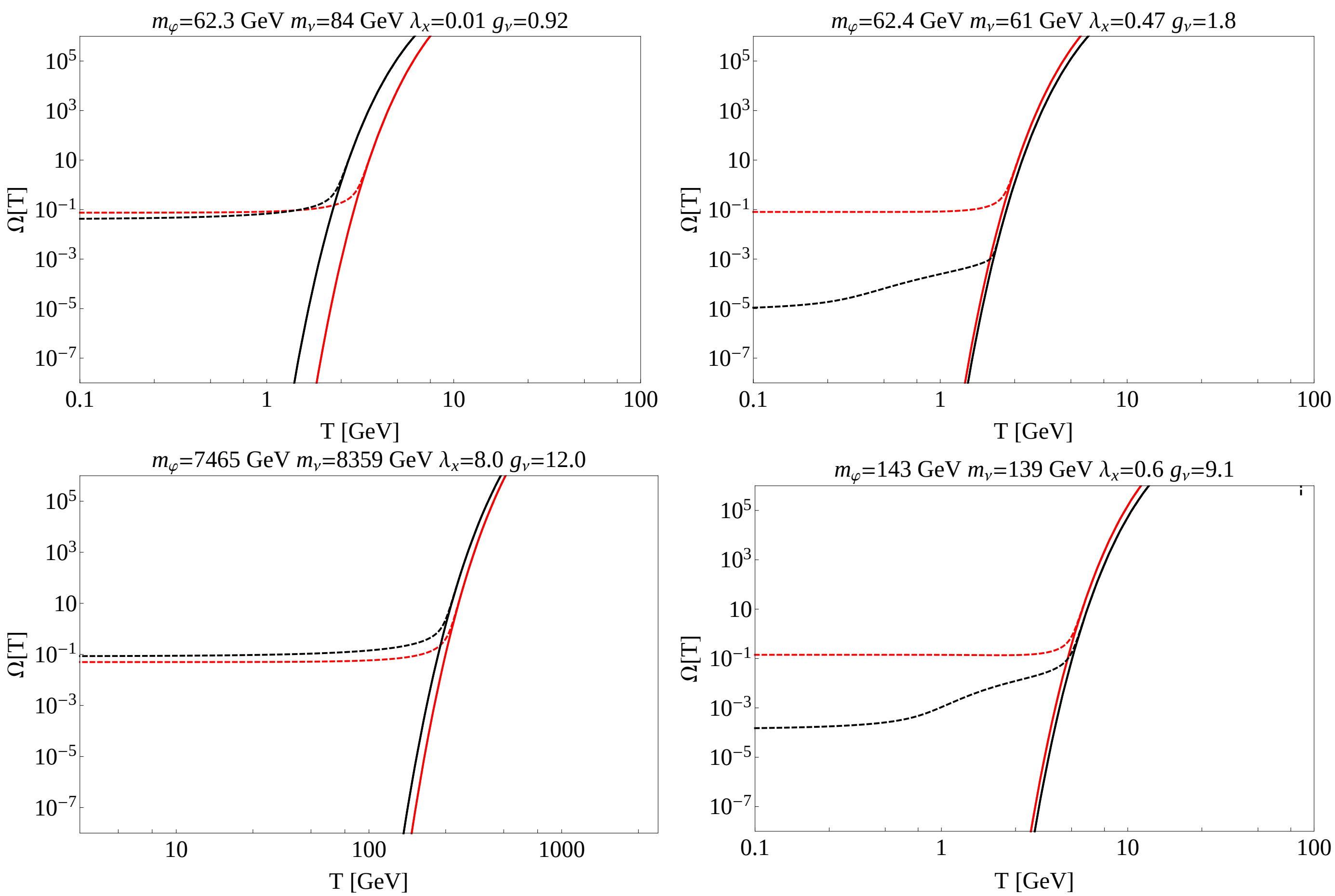

Figure 12: Selected solutions of the Boltzmann equation for parameters that satisfy both WMAP and XENON constraints.

Conclusions

- The two-component DM model made of φ and ν was discussed.

- Solutions consistent with $\Omega_{DM}h^2$ and $\sigma_{\rm DM-N}$ were found for

  - $m_\varphi \simeq \frac{m_{Higgs}}{2}$: $\Omega_\varphi > \Omega_\nu$, $m_\nu \lesssim m_\varphi$, $\lambda_x \gtrless 0$
  - $m_\varphi \sim 130 - 140$ GeV: $\Omega_\varphi > \Omega_\nu$, $m_\nu \lesssim m_\varphi$, $\lambda_x < 0$
  - $m_\varphi \gtrsim 3$ TeV: $\Omega_\varphi < \Omega_\nu$, $m_\nu > m_\varphi$, $\lambda_x > 0$

- In order to enhance the annihilation rate for ν, large values of the $\nu - \varphi$ coupling $g_\nu \simeq 1 - 12$ are favored by the WMAP data.

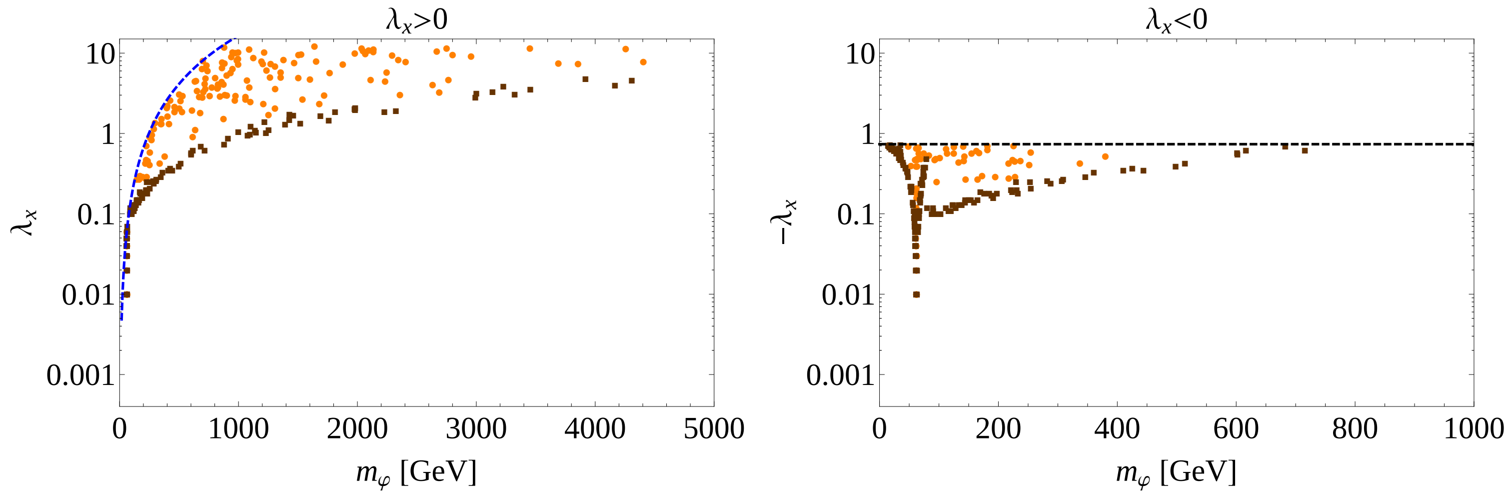

Figure 13: Points that satisfy WMAP bound within 6σ range projected into (λ_x, m_φ) plane. Orange circles - points where $\Omega_\varphi < \Omega_\nu$, dark orange squares - points where $\Omega_\varphi > \Omega_\nu$. The left panel corresponds to the solutions for positive λ_x, while the right panel is for negative λ_x. Blue dashed line is the consistency limit on λ_x, while the black horizontal dashed line is the stability limit $\lambda_\varphi = 8\pi$.

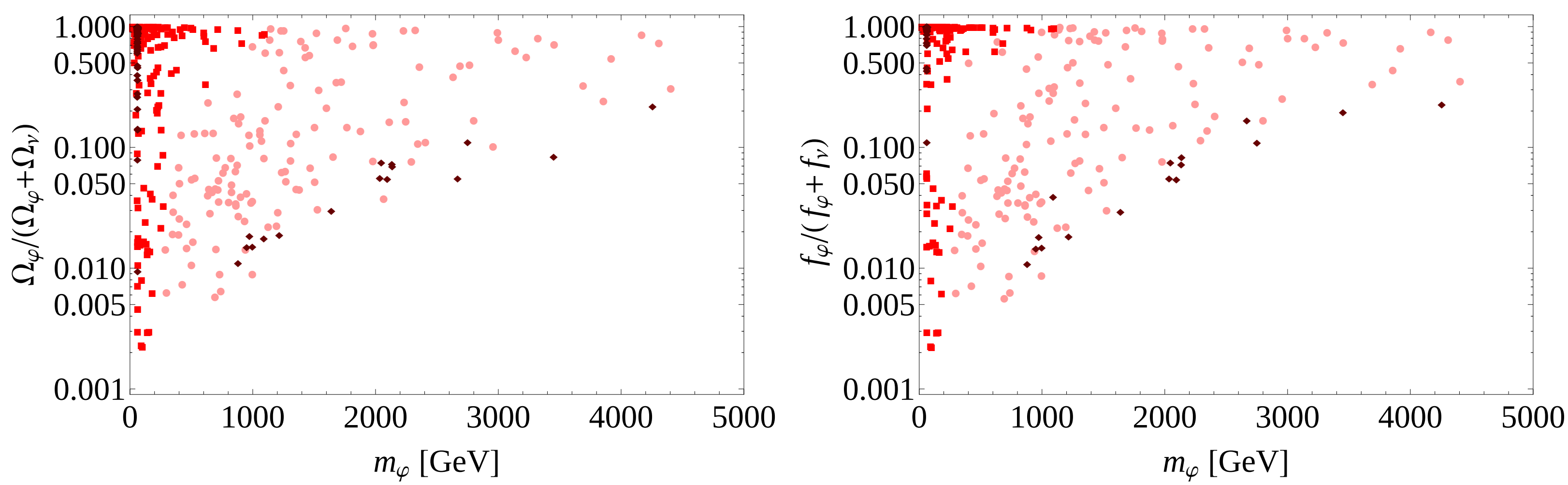

Figure 14: Relative abundance of φ (left panel) and relative number density of φ (right panel) as a function of m_φ for points that satisfy WMAP bound within 6σ. Light red points: $1 < \lambda_x < 10$; red points: $.1 < \lambda_x < 1$; dark red points: $\lambda_x < .1$